

# The Stellar Content of Obscured Galactic Giant HII Regions V: G333.1–0.4

E. Figuerêdo<sup>1</sup>

*IAG–USP, R. do Matão 1226, 05508–900, São Paulo, Brazil*

lys@astro.iag.usp.br

R. D. Blum<sup>1</sup>

*Cerro Tololo Interamerican Observatory, Casilla 603, La Serena, Chile*

rblum@noao.edu

A. Damineli<sup>1</sup>

*IAG–USP, R. do Matão 1226, 05508–900, São Paulo, Brazil*

damineli@astro.iag.usp.br

and

P. S. Conti

*JILA, University of Colorado  
Campus Box 440, Boulder, CO, 80309*

pconti@jila.colorado.edu

## ABSTRACT

We present high angular resolution near–infrared images of the obscured Galactic Giant HII (GHII) region G333.1–0.4 in which we detect an OB star cluster. For G333.1–0.4, we find OB stars and other massive objects in very early evolutionary stages, possibly still accreting. We obtained *K*–band spectra of three stars; two show O type photospheric features, while the third has no photospheric features but does show CO 2.3  $\mu\text{m}$  band–head emission. This object is at least as hot as an early B type star based on its intrinsic luminosity and is surrounded by a circumstellar disc/envelope which produces near infrared excess emission. A number of other relatively bright cluster members also display excess emission in the *K*–band, indicative of disks/envelopes around young

---

<sup>1</sup>Visiting Astronomer, Cerro Tololo Inter–American Observatory, National Optical Astronomy Observatories, which is operated by Associated Universities for Research in Astronomy, Inc., under cooperative agreement with the National Science Foundation.

massive stars. Based upon the O star photometry and spectroscopy, the distance to the cluster is  $2.6 \pm 0.4$  kpc, similar to a recently derived kinematic (near side) value. The slope of the  $K$ -band luminosity function is similar to those found in other young clusters. The mass function slope is more uncertain, and we find  $-1.3 \pm 0.2 < \Gamma < -1.1 \pm 0.2$  for stars with  $M > 5 M_{\odot}$  where the upper and lower limits are calculated independently for different assumptions regarding the excess emission of the individual massive stars. The number of Lyman continuum photons derived from the contribution of all massive stars in the cluster is  $0.2 \times 10^{50} \text{ s}^{-1} < N_{LyC} < 1.9 \times 10^{50} \text{ s}^{-1}$ . The integrated cluster mass is  $0.9 \times 10^4 M_{\odot} < M_{cluster} < 1.2 \times 10^4 M_{\odot}$ .

*Subject headings:* HII regions — infrared: stars — stars: early-type — stars: fundamental parameters — stars: formation

## 1. Introduction

Massive stars have a strong impact on the evolution of Galaxies. O-type stars and their descendants, the Wolf-Rayet stars, are the main source of UV photons, mass, energy and momentum to the interstellar medium. They play the main role in the ionization of the interstellar medium and dust heating. The Milky Way is the nearest place to study, simultaneously, massive stellar populations and their impact on the surrounding gas and dust. The sun's position in the Galactic plane, however, produces a heavy obscuration in the visual window ( $A_V \approx 20 - 40$  mag) toward the inner Galaxy, where massive star formation activity is the largest. At longer wavelengths such as in the near infrared, the effect of interstellar extinction is lessened ( $A_K \approx 2 - 4$  mag), yet the wavelengths are still short enough to probe the stellar photospheric features of massive stars (Hanson et al. 1996).

The study of Giant HII regions (GHII – emitting at least  $10^{50}$  LyC photons  $\text{s}^{-1}$ , or  $\approx 10 \times$  Orion) in the near-infrared can address important astrophysical issues such as: 1. characterizing the stellar content by deriving the initial mass function (IMF), star formation rate and age; 2. determining the physical processes involved in the formation of massive stars, through the identification of OB stars in very early evolutionary stages, such as embedded young stellar objects (YSOs) and ultra-compact HII regions (UCHII); and 3. tracing the spiral arms of the Galaxy by measuring spectroscopic parallaxes for main sequence OB stars. The exploration of the stellar content of obscured Galactic GHII regions has been studied recently by several groups: Hanson et al. (1997), Blum et al. (1999, 2000, 2001), Figuerêdo et al. (2002) and Okumura et al. (2000). These observations revealed massive star clusters at the center of the HII regions which had been previously discovered and studied only at much longer radio wavelengths.

In this work, we present results for G333.1–0.4 (R.A. = 16h21m03.3s and DEC. = –50d36m19s J2000), located at a kinematic distance 2.8 kpc (near side) or 11.3 kpc (far side), which we adopted from Vilas-Boas & Abraham (2000) with  $R_0 = 7.9$  kpc. Inward of the solar circle the galactic

kinematic rotation models give two values for the distance. A difficulty with such models comes from the classical two-fold distance ambiguity for lines of sight close to the Galactic Center (GC) (Watson et al. 2003). Furthermore, non-circular velocity components can lead to erroneous distances. We will show below that a spectroscopic parallax method leads to a distance of  $2.6 \pm 0.4$  kpc. G333.1–0.4 does not appear in visible passband images, but in the infrared one sees a spectacular star formation region.

In the present paper, we present an investigation of the stellar content of G333.1–0.4 through the  $J$ ,  $H$  and  $K$  imaging and  $K$ -band spectroscopy (described in §2). In §3 we consider the photometry, and in §4 we analyze the spectra. We determine the distance in §5 and discuss the results in §6.

## 2. Observations and Data Reduction

$J$  ( $\lambda \approx 1.3 \mu\text{m}$ ,  $\Delta\lambda \approx 0.3 \mu\text{m}$ ),  $H$  ( $\lambda \approx 1.6 \mu\text{m}$ ,  $\Delta\lambda \approx 0.3 \mu\text{m}$ ) and  $K$  ( $\lambda \approx 2.1 \mu\text{m}$ ,  $\Delta\lambda \approx 0.4 \mu\text{m}$ ) images of G333.1–0.4 were obtained on the night of 1999 May 1 and a new set of images  $65''$  east of the cluster on the night of 2001 July 10. Both sets utilized the f/14 tip-tilt system on the Cerro Tololo Interamerican Observatory (CTIO) 4-m Blanco Telescope using the facility imager OSIRIS<sup>1</sup>. Spectroscopic data were acquired with the Blanco telescope in 2000 May 19, 21 and 22 and 2001 July 11. OSIRIS delivers a plate scale of  $0.16'' \text{ pix}^{-1}$ . All basic data reduction was accomplished using IRAF<sup>2</sup>. Each image was flat-fielded using dome flats and then sky subtracted using a median-combined image of five to six dithered frames. Independent sky frames were obtained  $5\text{--}10'$  south of the G333.1–0.4 cluster for direct imaging and  $1\text{--}2'$  west for spectroscopy.

### 2.1. Imaging

All images were obtained under photometric conditions. Total exposure times on 1999's run were 270s, 135s and 81s at  $J$ ,  $H$  and  $K$ , respectively. The individual  $J$ ,  $H$  and  $K$  1999's frames were shifted and combined. These combined frames have point sources with FWHM of  $\approx 0.63''$ ,  $0.54''$  and  $0.56''$  at  $J$ ,  $H$  and  $K$ , respectively. DoPHOT (Schechter et al. 1993) photometry was performed on the combined images. All reduction procedures and photometry were performed for each set of images (1999 and 2001) separately, and the resulting combined magnitudes were included in a single list. The 1999 images are deeper than the 2001 images, so we performed photometric completeness tests and corrections to each set of images independently (see below).

---

<sup>1</sup>OSIRIS is a collaborative project between Ohio State University and CTIO. Osiris was developed through NSF grants AST 90–16112 and AST 92–18449.

<sup>2</sup>IRAF is distributed by the National Optical Astronomy Observatories.

The flux calibration was accomplished with standard star GSPC S875–C (also known as [PMK98] 9170) from Persson et al. (1998) which is on the Las Campanas Observatory photometric system (LCO). The LCO standards are essentially on the CIT/CTIO photometric system (Elias et al. 1982), though color corrections exist between the two systems for the reddest stars. No transformation has been derived for OSIRIS and either CIT/CTIO or LCO systems. Figure 1 shows a finding chart using the  $K$ –band image made from combination of 1999 and 2001 observations. The area used to measure the sky counts is shown at the lower left.

The standard star observations were taken just after the G333.1–0.4 data acquisition and within 0.17 airmass from the target. The color correction and this remaining airmass will add uncertainties of the order of 2% in the worst case ( $J$ –band). No corrections were applied for this small difference in airmass between target and standard.

Aperture corrections for 16 pixel radius circles were used to put the instrumental magnitudes on a flux scale. Ten uncrowded stars on the G333.1–0.4 images were used for this purpose. In order to determine the zero point for the 2001 images we used stars in common with the 1999 images.

Uncertainties for the  $J$ ,  $H$  and  $K$  magnitudes in 1999 images include the formal DoPHOT error added in quadrature to the error in the mean of the photometric standard and to the uncertainty of the aperture correction used in transforming from the DoPHOT photometry to OSIRIS magnitudes. The sums in quadrature of the aperture correction and standard star uncertainties are  $\pm 0.010$ ,  $\pm 0.017$  and  $\pm 0.044$  mag in  $J$ ,  $H$  and  $K$ , respectively. The scatter in the instrumental magnitudes in the set of stars from the 1999 images used to calibrate the May 2001 images are  $\pm 0.04$ ,  $\pm 0.07$  and  $\pm 0.06$  mag in  $J$ ,  $H$  and  $K$ , respectively. Thus, the errors in the bright star magnitudes in 2001 images are dominated by this scatter. The mean of the final magnitudes errors including all objects detected are  $\pm 0.047$ ,  $\pm 0.049$  and  $\pm 0.078$  mag in  $J$ ,  $H$  and  $K$  respectively. We adopted an arbitrary cutoff of 0.2 mag (stars with larger errors were excluded from further analysis).

The completeness of DoPHOT detections was determined through artificial star experiments. This was accomplished by inserting fake stars in random positions of the original frame, and then checking how many times DoPHOT retrieved them. The PSF of the fake star was determined from an average of real stars found in isolation. Adding a large number of stars to the real images could effect the crowding. Instead, we chose to add a small number and repeat the test many times. We inserted a total of 24000 stars in the magnitude interval  $8 \leq K \leq 20$ , corresponding to twenty seven times the number of real stars recovered in the original DoPHOT run. For every  $\Delta K = 0.5$  we inserted simultaneously 10 stars in the  $K$ –band image (240 stars total), and then re–ran DoPHOT to see how many were recovered. This was repeated 100 times. The completeness of the sample is defined as the percentage of stars recovered in these tests. In Figure 3 we present the result of these experiments – the photometric completeness. The performance of the photometry is better than 92% for a 16th magnitude in the  $K$  band. The procedure above was repeated for the  $J$  and  $H$  bands and in the both cases the performance of the photometry is better than 92% for  $J < 16.5$  and  $H < 16.75$ . The right panel in the Figure 3 shows the differences between the input magnitudes of

the artificial stars and the output magnitudes of the artificial stars detected by DoPHOT. Using the magnitude limit (16.0), the difference between the input and output magnitude of the false stars is 0.044. This difference is similar to the instrumental uncertainties given by the DoPHOT. Although we show in Figure 3 only the results for the 1999 data set completeness test, the same experiment was performed for the offset images which have different depth. All data sets were corrected for completeness separately before constructing the combined luminosity function.

## 2.2. Spectroscopy

The  $K$ -band spectra of three of the brightest stars in the G333.1–0.4 cluster were obtained: #1, #2 and #4 with OSIRIS. One dimensional spectra were obtained by extracting and summing the flux in  $\pm 2$  pixel apertures. The extractions include local background subtraction from apertures,  $\approx 1''$  on either side of the object. Moreover, we used background apertures in order to subtract the uniform nebular component of emission from the target spectra.

Wavelength calibration was accomplished by measuring the position of bright OH lines from the  $K$ -band sky spectrum (Oliva & Origlia 1992). The spectra were divided by the average continuum of several B9V-type stars to remove telluric absorption. The airmass differences between objects and B9V-type star are  $< 0.05$  and no corrections were applied for these small differences.

The  $\text{Br}\gamma$  photospheric feature was removed from the average B9V-type star spectrum by eye by drawing a line between two continuum points. Since  $\text{Br}\gamma$  is free from strong telluric features, it is sufficient to cut off this line by eye by drawing a line between two continuum points, to obtain the template for telluric lines.  $\text{Br}\gamma$  does play a key role in classification of the cluster stars. The  $K$ -band classification scheme for OB stars is based on faint lines of CIV, HeI, NIII and HeII. Actually, the spectra of stars in HII region young are often contaminated by the  $2.058 \mu\text{m}$  HeI and  $\text{Br}\gamma$  nebular lines, but this is not important, since these lines are not necessary for classifying O-type stars (Hanson et al. 1996).

The spectral resolution at  $2.2 \mu\text{m}$  is  $R \approx 3000$  for OSIRIS and the linear dispersion is  $\lambda/\text{pix} \approx 3.6 \text{ \AA}/\text{pixel}$ .

## 3. Results: Imaging

The OSIRIS  $J$ ,  $H$  and  $K$ -band images reveal a rich, embedded star cluster readily seen on the right side of Figure 1, where the stellar density is higher than the area to the left. We detected a total of 866 stars in the  $K$ -band image of the cluster and the field located  $65''$  east. Of those 866 stars, 757 were detected also in the  $H$ -band and 343 in all three filters. We have not detected objects in  $J$  or  $H$  bands that was not picked up in  $K$  with magnitude errors lesser than the cutoff limit. The image measures  $1'.69 \times 2'.87$ , amounting to an area of  $\approx 4.75 \text{ arcmin}^2$  – ignoring the

two blank strips at top and bottom right. A false color image is presented in Figure 2, made by combining the three near infrared images and adopting the colors blue, green and red, for  $J$ ,  $H$ , and  $K$ , respectively. The bluest stars are likely foreground objects, and the reddest stars are probably  $K$ -band excess objects, indicating the presence of hot dust for objects recently formed in the cluster (background objects seen through a high column of interstellar dust would also appear red). The bright ridge of emission that can be seen in the figure crossing the central region of the cluster in the N–S direction is most likely due to  $\text{Br}\gamma$  emission arising from the ionized face of the molecular cloud from which the cluster has been born. Darker regions are seen to the west of the emission ridge in Figure 2. This geometry suggests a young cluster containing massive stars, now in the process of destroying the local molecular cloud.

The  $H - K$  versus  $K$  color magnitude diagram (CMD) is displayed in Figure 4. In §5 we will determine a spectroscopic parallax of 2.6 kpc for G333.4–0.1. The labels in all plots refer to the same star as in Figure 1. We can see two concentrations of objects in the CMD. The first one appears around  $H - K \approx 0.3$ , which corresponds to an extinction of  $A_K = 0.42 \text{ mag}$  ( $A_V \approx 4.2 \text{ mag}$ ) using the interstellar reddening curve of (Mathis 1990) (see below). This sequence represents foreground stars; the expected extinction for this position along the Galactic plane is  $A_V \approx 1.8 \text{ mag/kpc}$  or  $A_K \approx 0.18 \text{ mag/kpc}$  (Jonck-Sorensen & Knude 1994). The second concentration of objects appears around  $H - K = 0.8$  or  $A_K = 1.22 \text{ mag}$ , probably indicating the average color of cluster members. A number of stars display much redder colors, especially the brightest ones in the K-band. These objects are located  $H - K > 2.0$  or  $A_K = 3.2$ . The dashed vertical line indicates the position of the theoretical zero age main sequence (ZAMS; see Table 1 of Blum et al. (2000)) shifted to 2.6 kpc distance and with interstellar reddening  $A_K = 0.42 \text{ mag}$ . An additional local reddening of  $A_K = 0.80 \text{ mag}$  results in the ZAMS position indicated by the vertical solid line.

The  $J - H$  versus  $H - K$  color-color plot is displayed in Figure 5. In that diagram the solid lines, from top to bottom, indicate interstellar reddening for main sequence M-type (Frogel et al. 1978), O-type (Koornneef 1983) and T Tauri (Meyer et al. 1997) stars (dashed line). The solid vertical line between the main sequence M-type and O-type lines indicates the position of ZAMS. Asterisks indicate  $A_K = 0, 1, 2$  and  $3$  reddening values. Dots are objects detected in all three filters. The error bars in both figures refers to the final errors in the magnitudes and colors.

### 3.1. Cluster members

Until now, we have assumed that our sample of stars is composed only by clusters members (not contaminated by foreground or background stars). In fact, it is not an easy task to identify these two populations except through statistical procedures. All details of our procedure used to separate the cluster members from projected stars in the cluster direction can be seen in Figure 6. The left panel shows the CMD (Figure 4) binned in intervals of  $\Delta K = 1.0$  and  $\Delta(H - K) = 1.0$  and containing all stars (clusters members plus projected stars). We used the stars in the region indicated by the square on bottom left in (Figure 1) to define a field population. In this case, we

supposed that there are only foreground or background stars and no clusters members in this small area. The star counts inside this square were normalized by the relative areas projected on the sky and then binned in the same interval cited above (center panel in Figure 6). The stellar density in the field (center panel) was then subtracted from the CMD with all stars (left panel) in bins of magnitude and color intervals, resulting in a CMD without contamination by projected stars (statistically; see the right panel). In the case of negative counts that occur when the field values are bigger than the cluster due to statistical fluctuations, the counts are added to an adjacent bin that has a larger number of objects.

This procedure works well for foreground stars, since there are relatively few stars in the direction of the cluster. For the background stars, the situation is more complex. However, we believe the excess of field stars which might contaminate the cluster sample is relatively small, due to the high obscuration toward the cluster itself and the large density of cluster stars expected. Unfortunately we can not use this procedure to cut off projected stars from our CMD and/or CCD. However, we can use this result to correct the luminosity function from contamination by non-cluster members, taking into account not only the magnitude of the stars but also their colors.

### 3.2. Reddening and excess emission

We estimate the reddening toward the cluster from the extinction law:  $A_K \sim 1.6 \times E_{H-K}$  (Cardelli et al. (1989) and Mathis (1990)) and using an average intrinsic color  $H - K = -0.04$  from Koornneef (1983) for OB stars. The Cardelli et al. (1989) extinction law assume  $R_V = 3.1$ . The Cardelli et al. (1989) extinction law is not truly independent of environment for  $\lambda > 0.9 \mu\text{m}$ , as pointed out by Whitney et al. (2004). However, in the case of the  $J$ ,  $H$  and  $K$ -bands (Whitney et al. 2004, Figure 3), differences in the extinction law are small enough to be neglected in the present case. The stars brighter than  $K = 14$  have an average observed color of  $H - K = 0.8$ , corresponding to  $A_K = 1.22 \text{ mag}$  ( $A_V \approx 12.2 \text{ mag}$ ). The interstellar component of the reddening can be separated from that local to the cluster stars by using the foreground sequence of stars seen in the CMD diagram (Figure 5) at  $H - K \approx 0.3$ , as mentioned in §3. For G333.1–0.4, the foreground component is then  $A_K \approx 0.42$ , leaving a local component of  $A_K \approx 0.8 \text{ mag}$ . Regarding the foreground component, as mentioned in §3, the value that we have found ( $A_K \approx 0.42$ ) to agrees very well with the value estimated from Jonch-Sorenson, for the distance of 2.6 kpc ( $A_K \approx 0.47$ ).

In order to place the ZAMS in the CMD, we used the  $H - K$  colors from Koornneef (1983) and absolute  $K$  magnitudes from Blum et al. (2000). The ZAMS is represented by a vertical solid line in Figure 4, shifted to  $D = 2.6 \text{ kpc}$  and reddened by  $A_K = 0.42$  due to the interstellar component. When adding the average local reddening ( $A_K = 0.8$ ), the ZAMS line is displaced to the right and down, as indicated by the dashed lines. We cannot fix the position of the ZAMS, since there is a scatter in the reddening. The small group of relatively bright stars ( $K \sim 12$ ) in between these two lines, suggests that some of them, the bluer ones, could mark the position of the ZAMS.

Objects found to the right of the O–type stars reddening line in the CMD of Figure 5, shown as a solid diagonal line, have colors deviating from pure interstellar reddening. This is frequently seen in young star clusters and is explained by hot dust in the immediate circumstellar environment. We can estimate a lower limit to the excess emission in the  $K$ –band by supposing that the excess at  $J$  and  $H$  are negligible, and that the intrinsic colors of the embedded stars are that of OB stars. Indeed, assuming that our sample of stars is composed of young objects (not contaminated by foreground or background stars), any OB star would have an intrinsic color in the range  $(H - K)_\circ = 0.0 \pm 0.06$  mag (Koornneef 1983). Let us adopt for all objects in our sample the intrinsic colors of a B2 V star:  $(J - H)_\circ = -0.09$  and  $(H - K)_\circ = -0.04$  (Koornneef 1983). The error in the color index would be smaller than the uncertainty in the extinction law we are using for the interstellar extinction. From the difference between the observed  $J - H$  and the adopted B2 V intrinsic  $J - H$  color, we obtain the  $J$  band extinction by using the extinction law. In other words, in order to estimate a lower limit to the excess emission we have assumed the intrinsic colors of all stars that was detected in  $J$ ,  $H$  and  $K$ –bands to be that of a B2 V star. Assuming the color  $J - H$  is not strongly affected by circumstellar excess emission, we have determined the line of sight extinction to each star using the extinction law. We derive the intrinsic apparent magnitudes based on  $A_J$  and the intrinsic B2 V colors. The  $K$ –band excess emission is then derived as  $K_{exc} = K_\circ - (K - A_K)$  or simply, as the difference between the observed  $A_K$  and the  $A_K$  estimated from the  $J - H$  excess alone.

Our results are displayed in Figure 7. In this plot we have only included objects with measured  $J$ ,  $H$  and  $K$  magnitudes. The solid line indicate  $K_{exc} = 0$ . Connected solid diamonds refer to the average value of the  $K$  excess in 1 magnitude bins. Dashed lines indicate 1, 2 and 3  $\sigma$  from the average. Bright objects with very large excess in the upper right corner of Figure 7, cannot be explained by errors in the dereddening procedure because they have measured  $J$ ,  $H$ , and  $K$ . They could represent the emission from accretion disks around the less massive objects in the cluster. Objects such as #488, #472 and #416 are well above of the 3  $\sigma$  scatter for otherwise normal stars.

Most of the stars in Figure 7 have a modest negative excess, about  $-0.2$  magnitude. This negative excess is a consequence of our assumption that all stars have the intrinsic color of a B2 V type star and is thus not physical. With reference to Figure 5, one can see that any star which lies above the reddening line for a B2 V must, by definition, have a negative excess under the assumption that the excess emission is in the  $K$ –band and the intrinsic photospheric colors are that for a B2 V star. Our goal is to identify stars with a significant excess which would cause them to lie to the right of reddening line in Figure 5, so this modest negative excess for “normal” stars, or stars with a small excess is not important for our purposes.

In Figure 7, the magnitude of the large excess (almost two mag for object #6) is in agreement with the values found by Hillenbrand & Carpenter (2000) for young stars in the Orion cluster. In the following sections we have only corrected the  $K$ –excess for stars with positive excess as determined here, for all others we impose zero excess emission. Low mass YSOs have typical excess of several 10th’s of a magnitude (Hillenbrand & Carpenter 2000), depending on the age of the cluster.

### 3.3. The KLF and the IMF

After correcting for non-cluster members, interstellar reddening, excess emission (a lower limit) and photometric completeness, the resulting  $K$ -band luminosity function ( $KLF$ ) is presented in Figure 8. A linear fit (solid line), excluding deviant measures by more than  $3\sigma$ , has a slope  $\alpha = 0.24 \pm 0.02$ . A considerably steeper KLF slope was obtained for W42 ( $\alpha = 0.40$ ) by Blum et al. (2000) and for NGC3576 ( $\alpha = 0.41$ ) by Figuerêdo et al. (2002). A linear fit only using stars measured in all filters  $J$ ,  $H$  and  $K$  (dashed line in Figure 8) results in a slope very close to that found including all stars ( $\alpha = 0.26 \pm 0.04$ ). The coincidence is not surprising, since the fitting in both cases is dominated by the objects detected in the three filters.

We can evaluate the stellar masses by using Shaller et al. (1992) models, assuming that the stars are on the ZAMS instead of the pre-main sequence. This is a reasonable approximation for massive members of such a young cluster. Stars more massive than about  $M = 5M_{\odot}$  should be on the ZAMS according to the pre-main sequence (PMS) evolutionary tracks presented by Siess et al. (2000). The main errors in the stellar masses, given this restriction, will be due to the effects of circumstellar emission and stellar multiplicity. Our correction to the excess emission is only a lower limit, since we assumed the excess was primarily in the  $K$  band (but according to Figure 7, there are not many stars with large excess for the higher masses). Hillenbrand et al. (1992) have computed disk reprocessing models which show the excess in  $J$  and  $H$  can also be large for disks which reprocess the central star radiation. An underestimate of the excess emission will result in an overestimate of the mass for any given star and the cluster as a whole. The slope of the mass function should be less effected. It is difficult to quantify the effect of binarity on the IMF. If a given source is binary, for example, its combined mass would be larger than inferred from the luminosity of a “single” star and its combined ionizing flux would be smaller. The cluster total mass would be underestimated, the number of massive stars and the ionizing flux would be overestimated. The derived IMF slope would be flatter than the actual one.

With these limitations in mind, we have transformed the KLF into an IMF. Since other authors also do not typically correct for multiplicity, our results can be inter-compared, as long as this parameter doesn’t change from cluster to cluster. The IMF slope derived for G333.1–0.4 is  $\Gamma = -1.1 \pm 0.2$ , which is flatter than Salpeter’s slope ( $1.5 \sigma$  from his value - Salpeter (1955)). Figure 9 shows the binned magnitudes from Figure 8 transformed into masses (triangles) and the fit to these points considering all objects more massive than  $M = 5.0 M/M_{\odot}$  (solid line). The dashed line in the figure indicates a fit for the case of only those objects more massive than  $M = 5.0 M/M_{\odot}$  which have  $JHK$  magnitudes measured. The fit ( $\Gamma = -1.0 \pm 0.2$ ) is very close to that derived for all stars. Our result depends on the calculation of the excess emission which is uncertain. In the following section, we show that different assumptions on the excess emission lead to an IMF slope which is consistent with Salpeter’s slope.

Massey et al. (1995) made a comparison between IMF’s of Galactic and LMC OB associations/clusters and no significant deviation was found from Salpeter’s value. A steeper IMF slope

was obtained for the Trapezium cluster ( $\Gamma = -1.43 \pm 0.10$ ) by Hillenbrand & Carpenter (2000) and for NGC3576 ( $\Gamma = -1.62 \pm 0.12$ ) by Figuerêdo et al. (2002). Flatter slopes have been reported only for a few clusters, most notably the Arches and Quintuplet clusters (Figer et al. 1999), both near the Galactic Center. Flatter slopes may indicate that in the inner Galaxy star forming regions the relative number of high mass to the low mass stars is higher than elsewhere in Galaxy. It is also possible that dynamical effects may be more important in the inner Galaxy. Portegies Zwart et al. (2001) have modeled the Arches cluster data with a normal IMF, but include the effects of dynamical evolution in the presence of the Galactic center gravitational potential. They find the observed counts are consistent with an initial Salpeter-like IMF.

We can determine an approximate lower limit to the total mass of the cluster by integrating the IMF between  $5 < M/M_{\odot} < 90$ . The upper integration limit corresponds to the mass of a O3-type star as given by Blum et al. (2000). The integrated cluster mass is  $M_{cluster} = (1.2 \pm 0.5) \times 10^4 M_{\odot}$ . To the extent that excess emission is underestimated for these stars, this lower limit to the cluster mass is overestimated.

The number of Lyman continuum photons derived from the IMF (Figure 9) was calculated from the contribution of all massive stars in the cluster. The Lyman continuum flux comes from the brightest stars which are well above our completeness limit. The intervals of masses in the IMF have been transformed into Lyman continuum flux by using results from Vacca et al. (1996) for stars more massive than  $18 M_{\odot}$ . We obtain the value for the total NLyc as  $1.9 \times 10^{50} s^{-1}$ . Our new spectrophotometric distance (see below) and that recently derived from radio observations (see §1) put G333.4–0.1 on the near side of the Galactic center; Smith et al. (1978) had estimated the NLyC based upon the far side distance.

### 3.4. Embedded Young Stellar Objects

As we can see in Figures 4, 5 and 7, some objects in G333.1–0.4 are very bright, display much redder colors and have excess emission. This is the case for objects such as #4, #6, #9, #13, #14, #598. In NGC3576 (Figuerêdo et al. 2002) we found 4 objects with photometric evidence for circumstellar emission, and whose spectra displayed either CO absorption or emission. Star #4 in the present sample also shows such a signature (see the following section), namely CO band head emission.

We can estimate the intrinsic properties of these YSOs by correcting for the excess emission and reddening evident in the photometric data of the color–magnitude diagram. In Table 1, we summarize the properties of these YSOs with excess emission and extinction as determined in §3.2 (only  $K$ -band excess). In each case, the local reddening is larger than the mean reddening that we found above for the cluster. The last two columns in the Table 1 display the spectral type and corresponding masses of these stars.

Given such evidence for circumstellar disks, we attempt to estimate an excess emission using

Hillenbrand et al. (1992) models for reprocessing disks to get a sense for how much bigger the excess might be compared to that derived by assuming all the excess is in the  $K$ -band. By starting with the maximum excess emission  $\Delta K = 4.05$  valid for a O7-type star (Hillenbrand et al. (1992) Table 4: all excess emission values are for face on line of sight) we derive the corresponding  $M_K$ . Using the ZAMS properties from Blum et al. (2000) Table 1, we obtain the corresponding stellar spectral type and mass. This is generally much smaller than the O7-type with which we started; the excess is obviously overestimated and the new luminosity and mass are underestimated. From this smaller mass, we use the corresponding excess emission and find a higher mass and luminosity. We iterate this procedure until convergence. This was done for all the stars listed in Table 1, and the results are given in Table 2. The resultant reddening was determined in the same way as for Table 1, except that now we have included the excess in the  $H - K$  color due to the Hillenbrand et al. (1992) reprocessing disks (nearly constant and equal to 0.5 mag).

The values in Tables 1 & 2 give a rough indication of the range of excesses that might be present, though neither is fully correct. The values in table 2 don't account for accretion luminosity nor for the inclination of the disk, while those derived only with photometric data assume negligible excess at  $J$  and  $H$ . A similar procedure using  $JHK$  photometry was adopted for two stars of NGC3576 (Figuerêdo et al. 2002). Barbosa et al. (2003) inferred similar spectral types from mid-infrared imaging techniques.

Although the Table 2 values are not true upper limits, since they don't account for accretion and may be too extreme if the disk we see is highly inclined, we can use them as a plausible “large excess” case. We used these assumptions on the excess, adopting the masses of the objects shown in Table 2, in order to compare to those from the previous IMF estimate (Figure 9). The slope in the case of the “large excess” is  $\Gamma = -1.3 \pm 0.2$  which is similar than Salpeter's slope ( $0.25 \sigma$  from his value - Salpeter (1955)).

New masses, derived from “large excess” correction, lead to a  $N_{\text{Lyc}} = 0.2 \times 10^{50} \text{s}^{-1}$ . This is smaller than the number of Lyman continuum photons detected from radio observations ( $0.6 \times 10^{50} \text{s}^{-1}$  at our derived distance). However, the observed  $N_{\text{Lyc}}$  photons by radio techniques is only a lower limit of that emitted by the stars, since some of them are destroyed by dust grains or leaked through directions of low optical depth. In this way, we can define the lower limit to the IMF slope as  $\Gamma < -1.3$ . The integrated cluster mass in this case is  $M_{\text{cluster}} > 0.9 \times 10^4 M_{\odot}$ .

### 3.5. G333.1-0.4 #18

In Figure 7 we have only included objects with measured  $J$ ,  $H$  and  $K$  magnitudes, but object #18 was not detected in the  $J$  band, and for this reason needs to be discussed separately. This object is bright and has the reddest color and largest excess in the cluster ( $K = 12.46$  and  $H - K = 5.74$ ). Figure 10 shows this object in the  $J$ ,  $H$  and  $K$  bands respectively. The  $K$ -band contours are over-plotted on the  $J$  and  $H$  images for comparison. Figure 10 demonstrates that source #18

is extremely red and suggests that this object is a deeply buried YSO.

Object #18 probably is a YSO that is consistent with an O-type star. A similar object was located in W51 (IRS3 from Goldader & Wynn-Williams (1994)). This object has a  $K$ -excess  $> 4.05$  when using the model with a reprocessing disk (Hillenbrand et al. 1992). Certainly, this is an object which deserves further study at longer wavelengths and could aid in trying to understand the processes involved in the formation of massive stars.

#### 4. Results: Analysis of Spectra

The spectra of sources #1 and #2 are shown in Figure 11 and source #4 is presented in Figure 12. Sources #1 and #2 have been divided by a low-order fit to the continuum after correction for telluric absorption. The signal-to-noise ratio is  $S/N > 80$  for each of these objects. These spectra have been background subtracted with nearby ( $\approx 1''.0$ ) apertures, though non-uniform extended emission could affect the resulting He I and  $Br\gamma$  seen in the stars themselves.

##### 4.1. O-star spectra

The spectra of sources #1 and #2 may be compared with the  $K$ -band spectroscopic standards presented by Hanson et al. (1996). The features of greatest importance for classification are (vacuum wavelengths) the CIV triplet at 2.0705, 2.0769 and 2.0842  $\mu\text{m}$  (emission), the NIII complex at 2.116  $\mu\text{m}$  (emission), and HeII at 2.1891  $\mu\text{m}$  (absorption). The 2.0842  $\mu\text{m}$  line of CIV is typically weak and seen only in very high signal-to-noise spectra (Hanson et al. 1996). The present classification system laid out by Hanson et al. (1996) does not have strong luminosity-class indicators. Still, the HeI (2.0581  $\mu\text{m}$ ) and  $Br\gamma$  (2.1661  $\mu\text{m}$ ) features can be used to approximately distinguish between dwarfs plus giants on the one hand, and supergiants on the other. Generally strong absorption in  $Br\gamma$  is expected for dwarfs and giant stars and weak absorption or emission for supergiants.

The presence of NIII and HeII in the spectrum of source #1 (see Figure 11) leaves no doubt that this is a O-type star. The CIV emission places the source #1 in the kO5–O6 subclass. The apparent absorption feature at the position of  $Br\gamma$  and of HeI suggest that source #1 probably is a dwarf or a giant star. The closest match in Hanson et al. (1996) atlas is star HD 93130 classified as O6III(f). However, it is very difficult to be sure about the exact luminosity class. In our earlier work, we adopted a ZAMS classification due to the presence of massive YSOs in the cluster. Following the same reasoning, we classify object #1 as O6V.

The spectrum of source #2 shows HeI at 2.0581  $\mu\text{m}$  (emission), HeI at 2.1137  $\mu\text{m}$  (weak absorption), NIII at 2.116  $\mu\text{m}$  (emission) and  $Br\gamma$  (2.1661  $\mu\text{m}$ ) in absorption. The presence of HeI and the absence of the CIV triplet indicate that this star is cooler than source #1 and a comparison with the Hanson’s standards gives an O8V type star. In any way, as we said in §2.2, the spectra

of stars in HII region are often contaminated by the  $2.058 \mu\text{m}$  HeI and  $\text{Br}\gamma$  nebular lines. In the source #1 it is not so critical but, in the case of source #2 it will deserves better  $S/N$  spectra to say definitively its spectral type.

#### 4.2. G333.1–0.4 #4

The spectrum of G333.1–0.4 #4 is shown in Figure 12. This object doesn't show photospheric lines, indicating that it is still (at least partially) enshrouded in its birth cocoon. This is corroborated by the excess emission derived from photometry (see Table 1 and Figure 5).

The CO band head at  $2.2935 \mu\text{m}$  appears in emission, and it is usually attributed to warm ( $> 1000\text{K}$ ), very dense ( $\rho \approx 10^{10} \text{ cm}^{-3}$ ) circumstellar material near the star (Scoville et al. 1983; Carr 1989). However, a variety of mechanisms and models have been proposed to explain the origin of CO emission in YSOs. These include circumstellar disks, stellar or disk winds, magnetic accretion mechanisms such as funnel flows, and inner disk instabilities similar to those which have been observed in FU Orionis-like objects and T Tauri stars in a phase of disk accretion (Carr 1989; Carr et al. 1993; Chandler et al. 1993; Biscaya et al. 1997). Hanson et al. (1997) reported the presence of CO in emission in several massive stars in M17 and Figuerêdo et al. (2002) also found CO emission in a massive YSO in NGC3576 as mentioned previously. A high resolution spectrum of source #4 is presented by Blum et al. (2004) who show that the emission is consistent with a disk origin.

### 5. Distance Determination

In the previous section we classified the spectra of two brightest stars in G333.1–0.4 as O type stars (O6 and O8). We can now estimate the distance to G333.1–0.4 by using the spectroscopic and photometric results. We compute distances assuming the O stars shown in the Figure 11 are zero-age main-sequence (ZAMS) or in the dwarf luminosity class (i.e., hydrogen burning). The spectral type in each case is assumed to be O6 (star #1) and O8 (star #2). For the ZAMS case, the  $M_K$  is taken from Blum et al. (2000). For the dwarf case, the distance is determined using the  $M_V$  given by Vacca et al. (1996) and  $V - K$  from Koornneef (1983). The distance estimates are shown in Table 3. For the derived spectral types, we obtain distances of  $2.6 \pm 0.4$  and  $3.5 \pm 0.7$  kpc for the ZAMS and dwarf cases, respectively. The former value is to be preferred given the presence of massive YSOs in the cluster. The uncertainty quoted for the mean distance is the standard deviation in the mean of the individual distances added in quadrature to the uncertainty in  $A_K$  (250 – 500 pc).

Our distance estimates are in close agreement with the near distance given by Vilas-Boas & Abraham (2000): 2.8 kpc. Their distance was obtained by the radio recombination line velocity and Galactic rotation model. Smith et al. (1978) estimated the  $L_{\text{yc}}$  luminosity of G333.1–0.4 to be

$10.8 \times 10^{50} \text{ s}^{-1}$  assuming a far kinematic distance (10.7 kpc). Adopting our mean value of 2.6 kpc, as indicated by the spectroscopic parallax, considerably reduces the expected ionizing flux from the radio continuum measurements to  $0.6 \times 10^{50} \text{ s}^{-1}$ . This value is about three times smaller than the value of  $1.9 \times 10^{50} \text{ s}^{-1}$  derived from counting the individual stars and using the mass function (see §3.3 above).

## 6. Discussion and Summary

We have presented deep *J*, *H* and *K* images of the stellar cluster in G333.1–0.4 (Figure 2) and *K*–band spectra for three cluster members. Two of them have classic O star absorption lines. The spectrum of G333.1–0.4 #4 (Figure 12) doesn’t show photospheric lines but rather CO emission. These features indicate that it is still enshrouded in its birth cocoon and is perhaps surrounded by a circumstellar disk. The *K*–band excess emission displayed by objects #4, #6, #9, #13, #14, #18, #483, #488 and #158 is similar to objects found in other GIII regions. These objects appear to be still heavily enshrouded by circumstellar envelopes and/or disks. Object #18 is an extremely buried YSO, and it deserves followup observations at longer wavelengths to further investigate its nature.

The KLF and IMF were computed and compared with those of other massive star clusters. The slope of the *K*–band luminosity function ( $\alpha = 0.24 \pm 0.02$ ) is similar to that found in other young clusters, and the IMF slope of the cluster,  $-1.3 < \Gamma < -1.1$ , is consistent with Salpeter’s value within  $1.25 \sigma$ .

Spectral types of the newly identified O stars and the photometry presented here constrain the distance to G333.1–0.4, which was uncertain from earlier radio observations. Our measurements break the ambiguity in the distance determinations from radio techniques. Our value,  $2.6 \pm 0.4$  kpc, is consistent with the lower distance determined by Vilas–Boas & Abraham (2000) and implies in  $N_{\text{Lyc}} = 0.6 \times 10^{50} \text{ s}^{-1}$ , what is considerably lower than that adopted by Smith et al. (1978). The number of Lyman continuum photons derived from the contribution of all massive stars in the cluster is  $0.2 \times 10^{50} \text{ s}^{-1} < N_{\text{Lyc}} < 1.9 \times 10^{50} \text{ s}^{-1}$ . The integrated cluster mass is  $0.9 \times 10^4 M_{\odot} < M_{\text{cluster}} < 1.2 \times 10^4 M_{\odot}$ .

EF and AD thank FAPESP and CNPq for support. PSC appreciates continuing support from the National Science Foundation. We thank an anonymous referee for the careful reading of this paper and for the useful comments and suggestions which have resulted in a much improved version.

## REFERENCES

- Barbosa, C. L., Daminieli, A., Blum, R. D., Conti, P. S. 2003, *AJ*, 216, 2411.  
 Behrend, R. & Maeder, A. 2001, *A&A*, 373, 555

- Biscaya, A. M., Rieke, G. H., Narayanan, G., Luhman, K. L., Young, E. T. 1997,  
Blum, R. D., Daminieli, A., Conti, P. S. 1999, *AJ*, 117, 1392  
Blum, R. D., Conti, P. S., Daminieli, A. 2000, *AJ*, 119, 1860  
Blum, R. D., Daminieli, A., Conti, P. S. 2001, *AJ*, 121, 3149  
Blum, R. D., Barbosa, C. L., Daminieli, A., Conti, P. S., and Ridgway, S. 2004, in preparation.  
Cardelli, J. A., Clayton, G. C., Mathis, J. S. 1989, *ApJ*, 345, 245  
Carr, J. S. 1989, *ApJ*, 345, 522  
Carr, J. S., Tokunaga, A. T., Najita, J., Shu, F. H., & Glassgold, A. E. 1993, *ApJ*, 411, L37  
Carter, B. S., 1990, *MNRAS*, 242, 01  
Caswell, J. L., Batchelor, R. A., Forster, J. R., Wellington, K. J. 1989, *Australian J. Phys.*, 42, 331  
Caswell, J. L., Vaile, R. A., Ellingsen, S. P., Whiteoak, J. B., Norris, R. P., 1995, *MNRAS*, 272, 96  
Chandler, C. J., Carlstrom, J. E., Scoville, N. Z., Dent, W. R. F., & Geballe, T. R. 1993, *ApJ*, 412, L71  
Blum, R. D., & Conti, P. S. 2002, *ApJ*, 564, 827  
DePoy, D. L., Atwood, B., Byard, P., Frogel, J. A., & O'Brien, T., 1993, *Proc. SPIE*, 1946, 667  
De Pree, C. G., Nysewander, M. C., Goss, W. M. 1999, *AJ*, 117, 2902  
Elias, J. H., Frogel, J. A., Matthews, K., & Neugebauer, G., 1982, *AJ*, 87, 1029  
Figer, D. F., Kim, S. S., Morris, M., Serabyn, E., Rich, R. M., McLean, I. S., 1999a, *AJ*, 525, 750  
Figuierêdo, E., Blum, R. D., Daminieli, A., Conti, P. S. 2002, *AJ*, 124, 2739  
Frogel, J. A., Persson, S. E., Matthews, K., Aaronson, M. 1978, *ApJ*, 220, 75  
Goldader, J. D. & Wynn-Williams, C. G. 1994, *ApJ*, 433, 164  
Goss, W. M. & Radhakrishnan, V. 1969, *Astrophys. Lett.*, 4, 199  
Goss, W. M. & Shaver, P. A., 1970, *Australian J. Phys. Astroph. Suppl.*, 14, 1  
Hanson, M. M., Conti, P. S., Rieke, M. J. 1996, *ApJS*, 107, 281  
Hanson, M. M., Howarth, I. D., Conti, P. S. 1997, *ApJ*, 489, 698  
Hillenbrand, L. A., Strom, S. E., Vrba, F. J., & Keene, J. 1992, *ApJ*, 397, 613

- Hillenbrand, L. A., Carpenter, J. M., 2000, *ApJ*, 540, 236
- Houk, N. & Cowley, A. P. 1975 *Michigan Spectral Catalogue, Vol. 1 (Univ. Michigan: Ann Arbor)*
- Johnson, H. L. 1966, *ARA&A*, 04, 193
- Jonch-Sorensen, H. & Knude, J. 1994 *A&A*, 288, 139
- Jones, T. J. et al. 1993, *ApJ*, 411, 323
- Koornneef, J. 1983, *A&A*, 128, 84
- Lada, C. J., DePoy, D. L., Merrill, K. M., Gatley, I., 1991, *ApJ*, 374, 533
- Lada, C. J., Adams, F. C., 1992, *ApJ*, 393, 278
- Luhman, K. L., Rieke, G. H., Young, E. T., Cotera, A. S., Chen, H., Rieke, M. J., Schneider, G., & Thompson, R. 2000, *ApJ*, 540, 1016
- K. L. Luhman 2000, *ApJ*, 544, 1044
- Malagnini, M. L., Morossi, C., Rossi, L., Kurucz, R. L. 1986, *A&A*, 162, 140
- Martin, S.C. 1997, *ApJ*, 478, L33
- Massey, P., Johnson, K. E., DeGioia-Eastwood, K. 1995, *ApJ*, 454, 151
- Mathis, J. S. 1990, *ARA&A*, 28, 37
- McGee, R. X., Gardner, F. F., 1968, *Australian J. Phys.*, 21, 149
- McGee, R. X., Newton, L. M., 1981, *MNRAS*, 196, 889
- Meyer, M. R., Calvet, N., Hillenbrand, L. A. 1997 *AJ*, 114, 288
- Moorwood, A. F. M., & Salinari, P. 1981, *A&A*, 102, 197
- Okumura, S., Mori, A., Nishihara, E., Watanabe, E. & Yamashita, T. 2000, *ApJ*, 543, 799
- Oliva, E. & Origlia, L. 1992, *A&A*, 254, 466
- Persi, P., Roth, M., Tapia, M., Ferrari-Toniolo, M. Marenzi, A. R., 1994 *A&A*, 282, 474
- Persson, S. E., Murphy, D. C., Krzeminski, W., & Roth, M., 1998, *AJ*, 116, 2475
- Portegies Zwart, S. F., Makino, J., McMillan, S. L. W., & Hut, P. 2001, astro-ph/0102259
- Reid, M. J. 1993, *ARA&A*, 31, 345
- Salpeter, E. E. 1955, *ApJ*, 121, 161

- Schecter, P. L., Mateo, M. L., & Saha, A., 1993, *PASP*, 105, 1342
- Scoville, N., Kleinmann, S. G., Hall, D. N. B. & Ridgway, S. T. 1983, *ApJ*, 275, 201
- Schaller, G., Schaerer, D., Meynet, G., Maeder, A. 1992, *A&AS*, 96, 269
- Siess et al. 2000, *A*, 358, 593.
- Smith, L. F. 1978, *ApJ*, 327, 128.
- Vacca, W. D., Garmany, C. D., Shull, J. M. 1996, *ApJ*, 460, 914
- Vilas-Boas, J. W. S. & Abraham, Z. 2000, *A&A*, 355, 1115.
- Watson, C., Araya, E., Sewilo, M., Churchwell, E., Hofner, P., Kurtz, S. 2003, *ApJ*, 587, 714.
- White, G. J. & Phillips, J. P., 1983 *MNRAS*, 202, 255
- Whitney, B. A., Indebetouw, R., Babler, B. L., Meade, M. R., Watson, C., Wolff, M. J., Wolfire, M. G., Clemens, D. P., Bania, T. M., Benjamin, R. A., Cohen, M., Devine, K. E., Dickey, J. M., Heitsch, F., Jackson, J. M., Kobulnicky, H. A., Marston, A. P., Mathis, J. S., Mercer, E. P., Stauffer, J. R., Stolovy, S. R., Churchwell, E., 2004 *ApJS*, 154, 315.
- Wilson, T. L., Mezger, P. G., Gardner, F. F., Milne, D. K., 1970 *A&A*, 6, 364

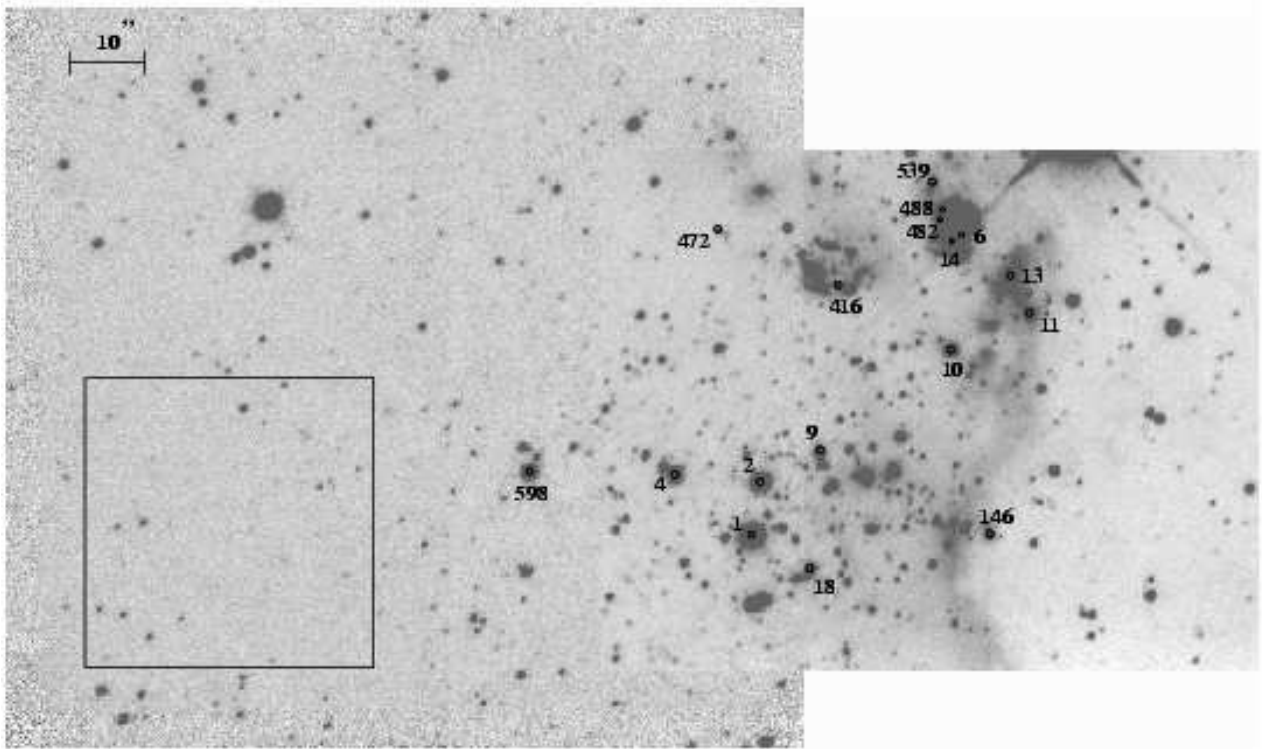


Fig. 1.— Finding chart using a  $K$ -band image of G333.1-0.4 plus a background field image  $65''$  east. The square (on the left) indicates the region that we used to define the background stars (see text). Object labels refer to the star names for all figures in this work. North is up and East to the left. The image measures  $1'.69 \times 2'.87$ , corresponding to an area of  $\approx 4.75 \text{ arcmin}^2$  after ignoring the two blank strips at top and bottom right.



Fig. 2.— False color image of G333.1-0.4: *J* is blue, *H* is green and *K* is red. The coordinates of the center of the image are RA (2000) = 16h21m03.3s and Dec. =  $-50^{\circ}36'19''$  and the size of the image is  $1.9' \times 1.7'$  (plate scale =  $0.16''/\text{pixel}$ ). North is up and East to the left.

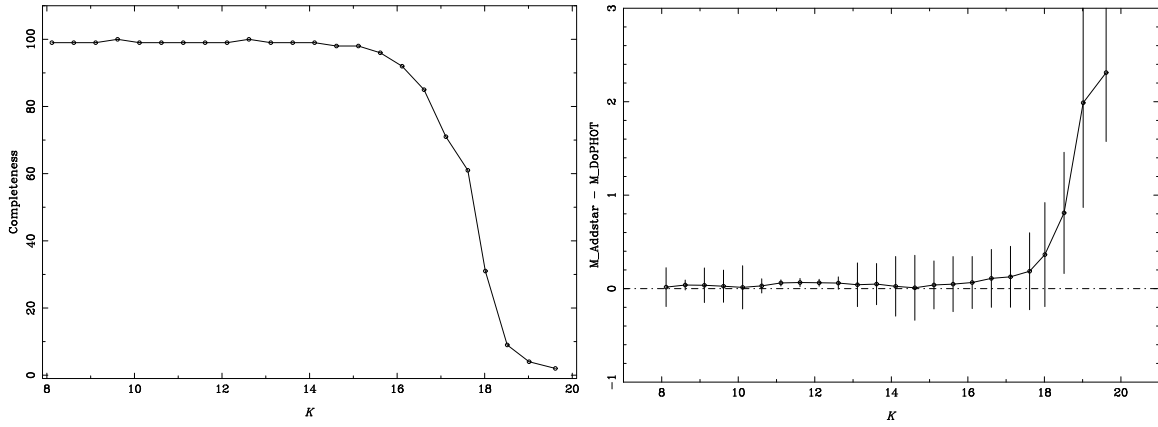


Fig. 3.— Derived completeness for the cluster photometry. The *left* panel shows the completeness (in percent detection) as derived from artificial star experiments (see text). The *right* panel displays the differences between the input magnitudes of the artificial stars and the output magnitudes as detected by DoPHOT (see text).

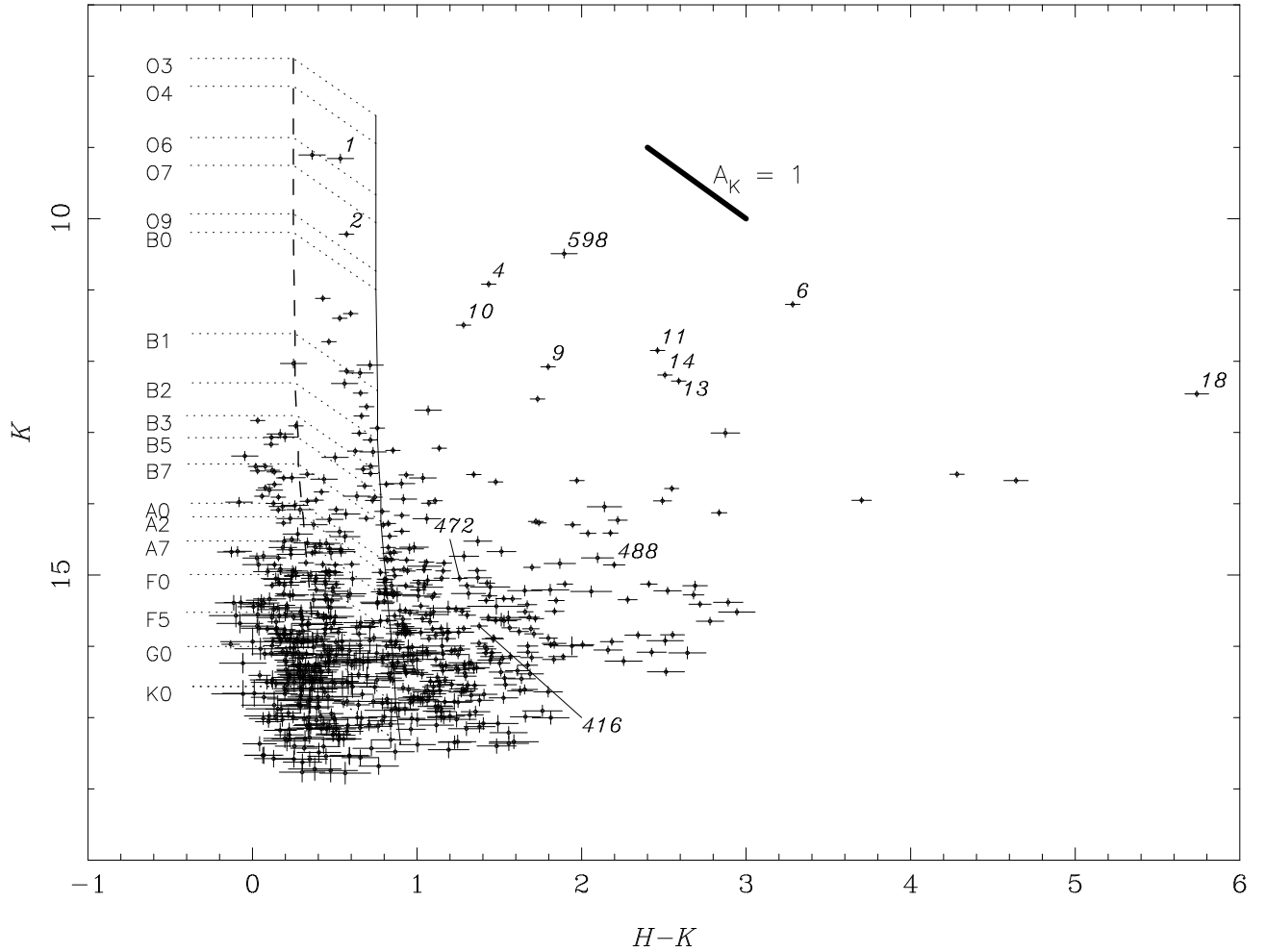


Fig. 4.—  $K$  vs  $H - K$  color-magnitude diagram (CMD). The left *dashed* line indicates the position of the theoretical ZAMS shifted to 2.6 kpc and with interstellar reddening  $A_K = 0.42 \text{ mag}$ . An additional “cluster” reddening component of  $A_K = 0.80 \text{ mag}$  ( $A_{Ktotal} = 1.22 \text{ mag}$ ) results in the ZAMS position indicated by the vertical *solid* line. Object number labels are the same as in Figure 1.

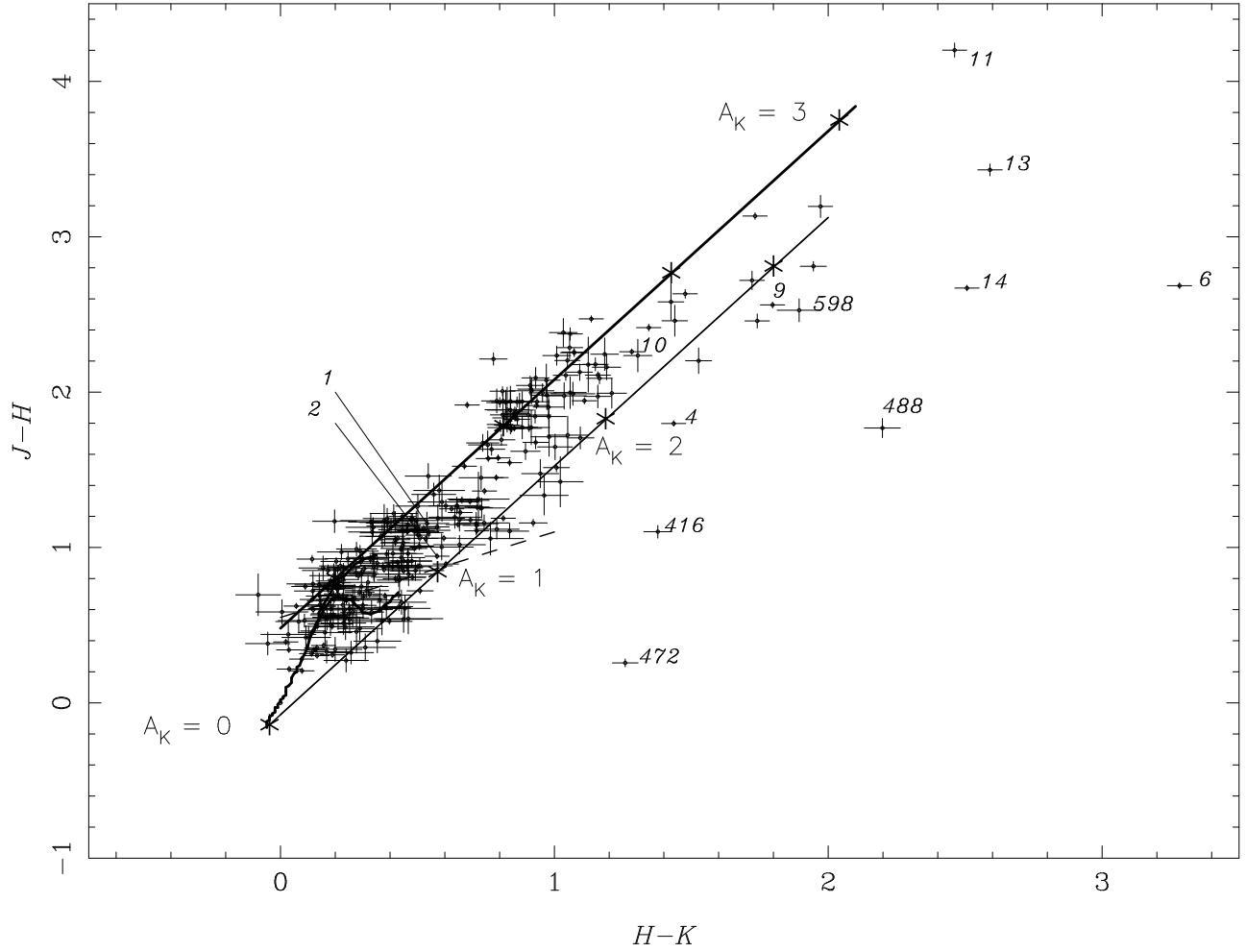


Fig. 5.—  $J-H$  vs  $H-K$  color-color plots showing the reddening line of M-type stars (*heavy solid line*), O-type stars (*solid line*) and T Tauri stars (*dashed line*). *Dots* refer to stars detected in the three filters. The *asterisks* indicate the corresponding  $A_K$  along the reddening vector.

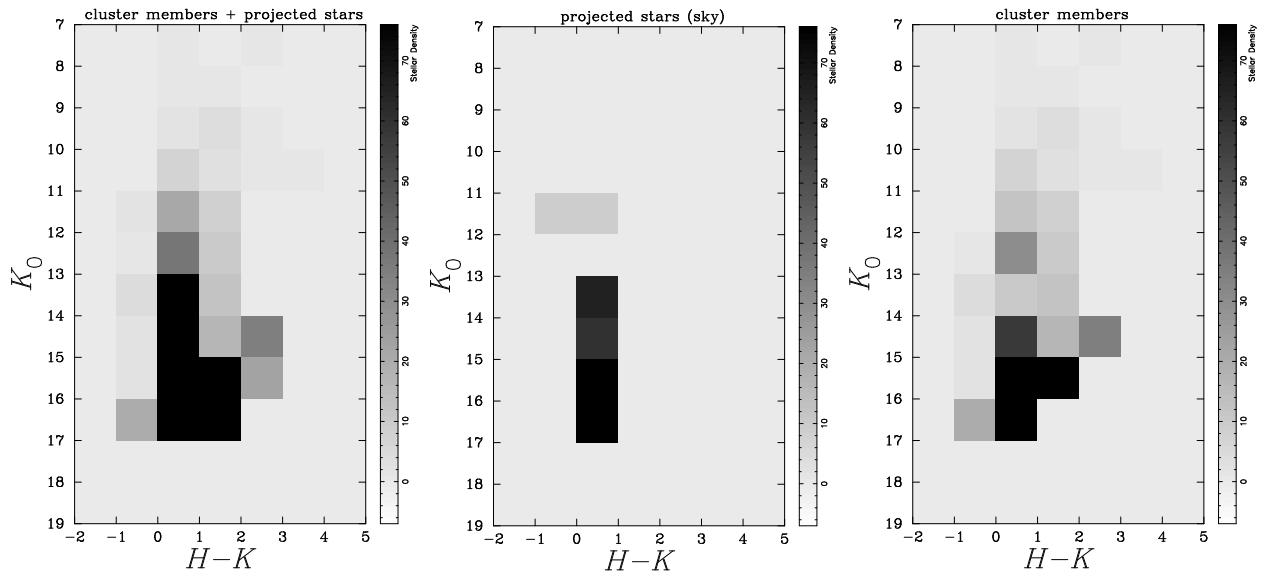


Fig. 6.— Color–Magnitude diagram binned in intervals of  $\Delta K = 1.0$  and  $\Delta(H - K) = 1.0$  in order to separate the cluster members from projected stars in the cluster direction. The complete CMD taking into account all stars is given in the *left* panel and the field CMD (represented by the square in Figure 1) in the *center* panel. The star counts were normalized by the relative areas projected on the sky. The *right* panel shows the cluster CMD obtained as the difference between the complete and field CMDs.

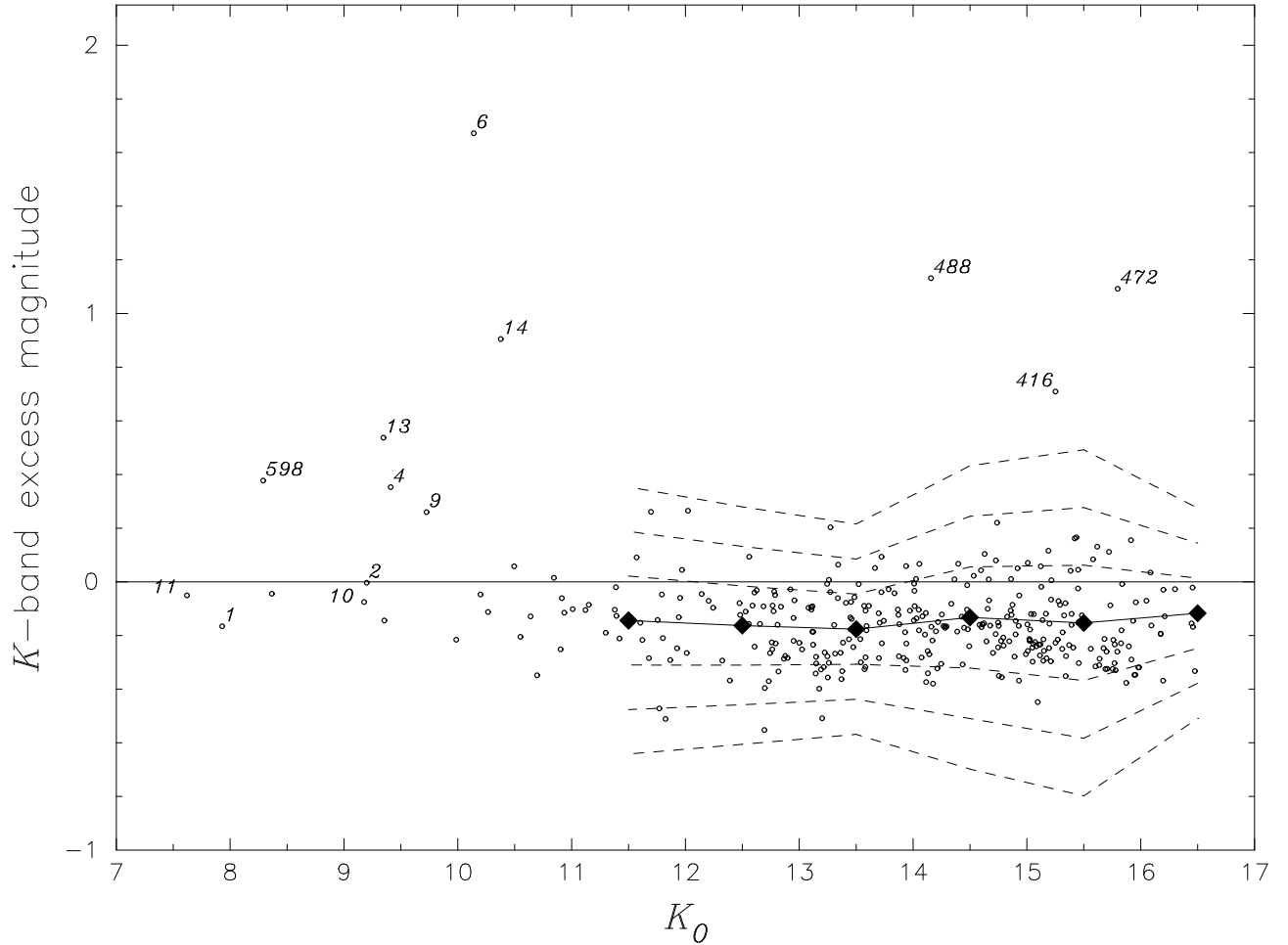


Fig. 7.— Excess emission as a function of dereddened  $K$ -band magnitude ( $K_0$ ). In this plot we have only included objects with measured  $J$ ,  $H$  and  $K$  magnitudes (dots). The solid line indicate  $K_{exc} = 0$ . Connected solid diamonds refer to the average value of the  $K$  excess in one magnitude bins. Dashed lines indicate one, two, and three  $\sigma$  from the average. Very positive values represent circumstellar emission.

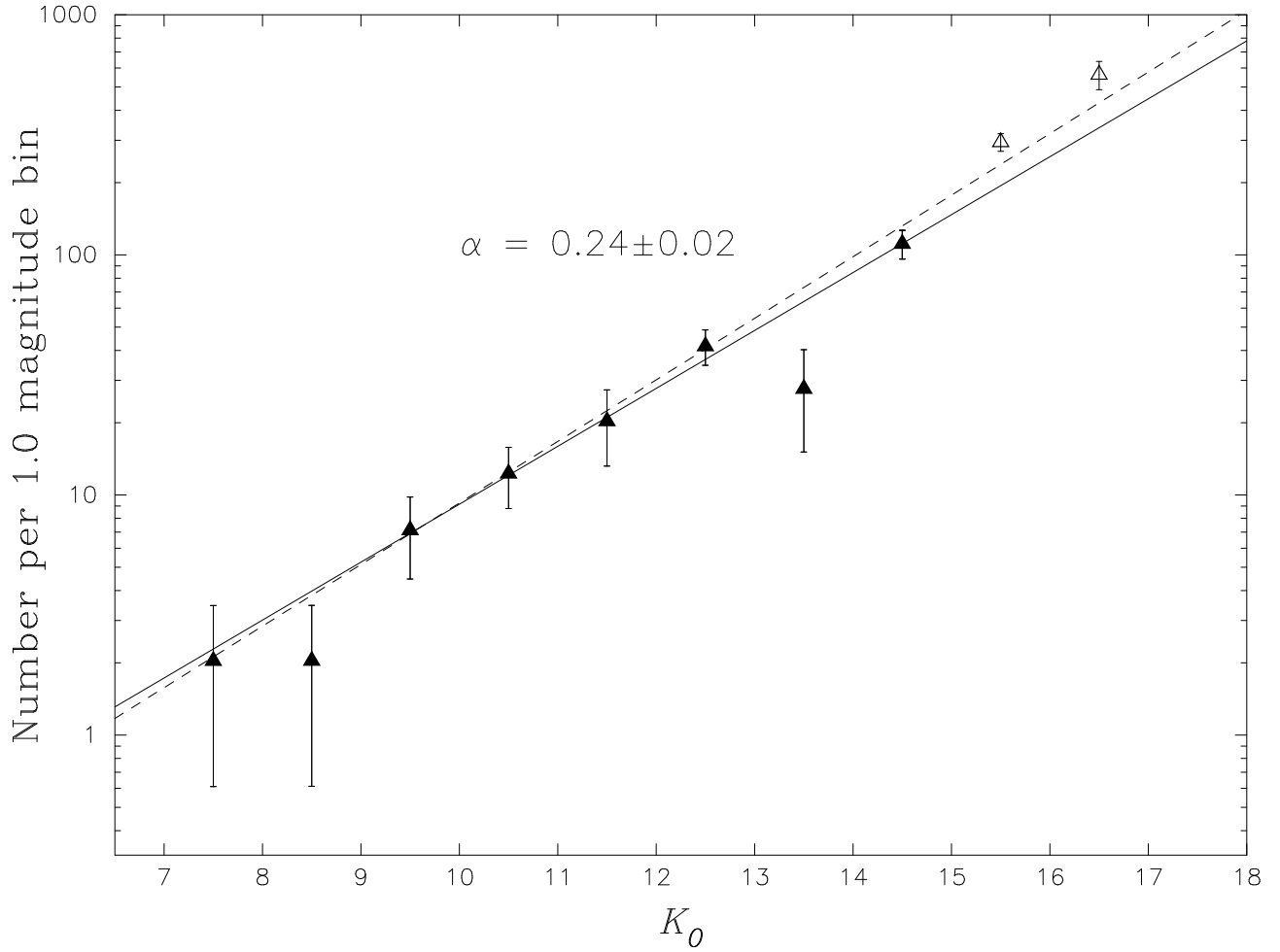


Fig. 8.— The  $K$ -band luminosity function of the cluster (cluster members CMD; see Figure 6 right panel), corrected for sample incompleteness.  $K_0$  is dereddened and corrected for excess emission; see text. A linear fit for stars measured in all filters (dashed line) results in a slope very similar to that found using all detected objects (*solid* line). Open triangles refer to bins that were not considered on the fit.

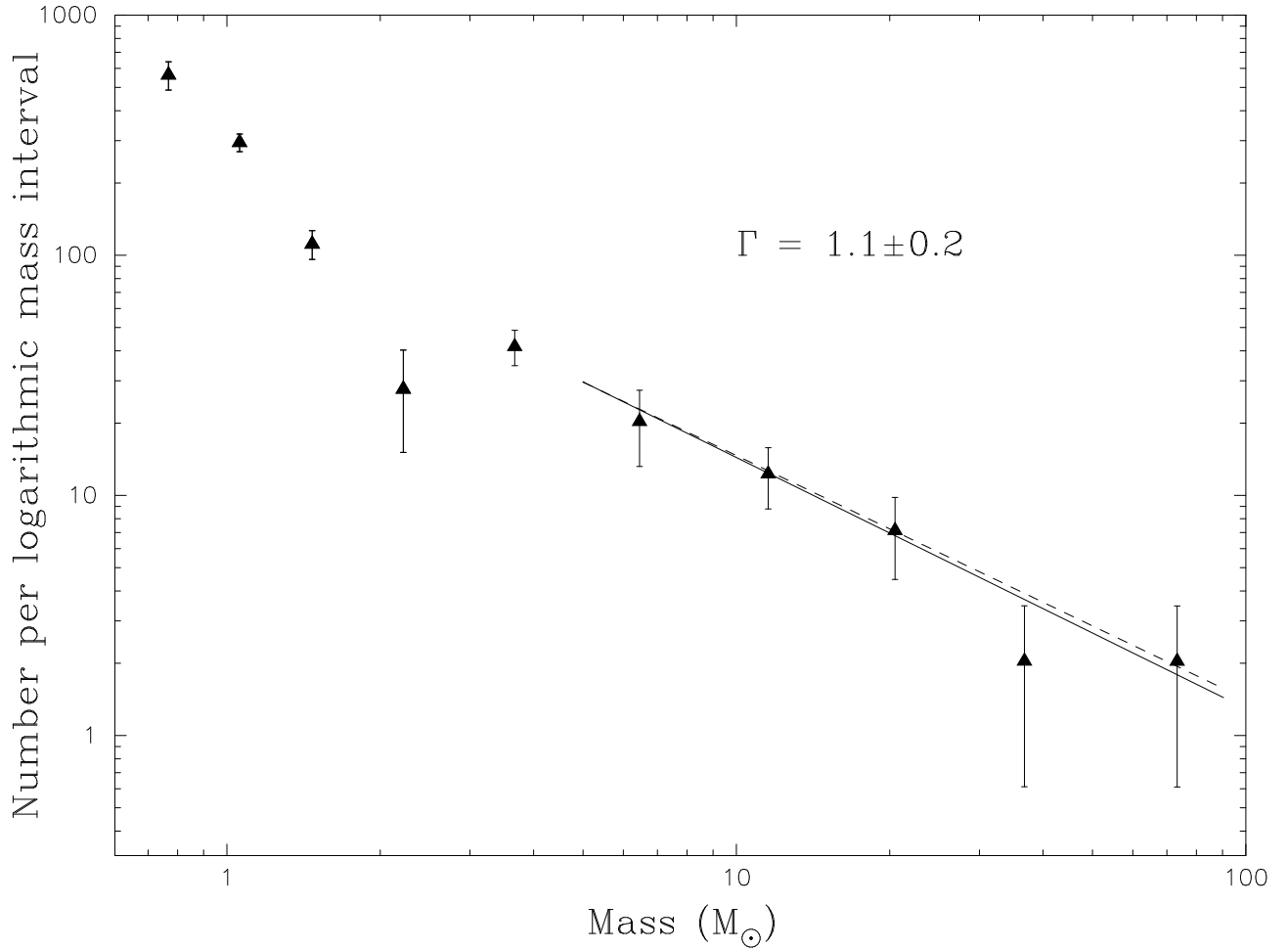


Fig. 9.— The IMF of the cluster members applying Shaller et al. (1992) models to the corrected  $K$ -band luminosity function from Figure 8. Using all stars in the sample, the best fit slope is  $\Gamma = -1.1 \pm 0.2$  (*solid* line), consistent with Salpeter (1955). Fitting only stars measured in all three filters (*dashed* line) results in a similar slope ( $\Gamma = -1.0 \pm 0.2$ ). Only stars with  $M > 5 M_{\odot}$  are used in determining the mass function slope; see text.

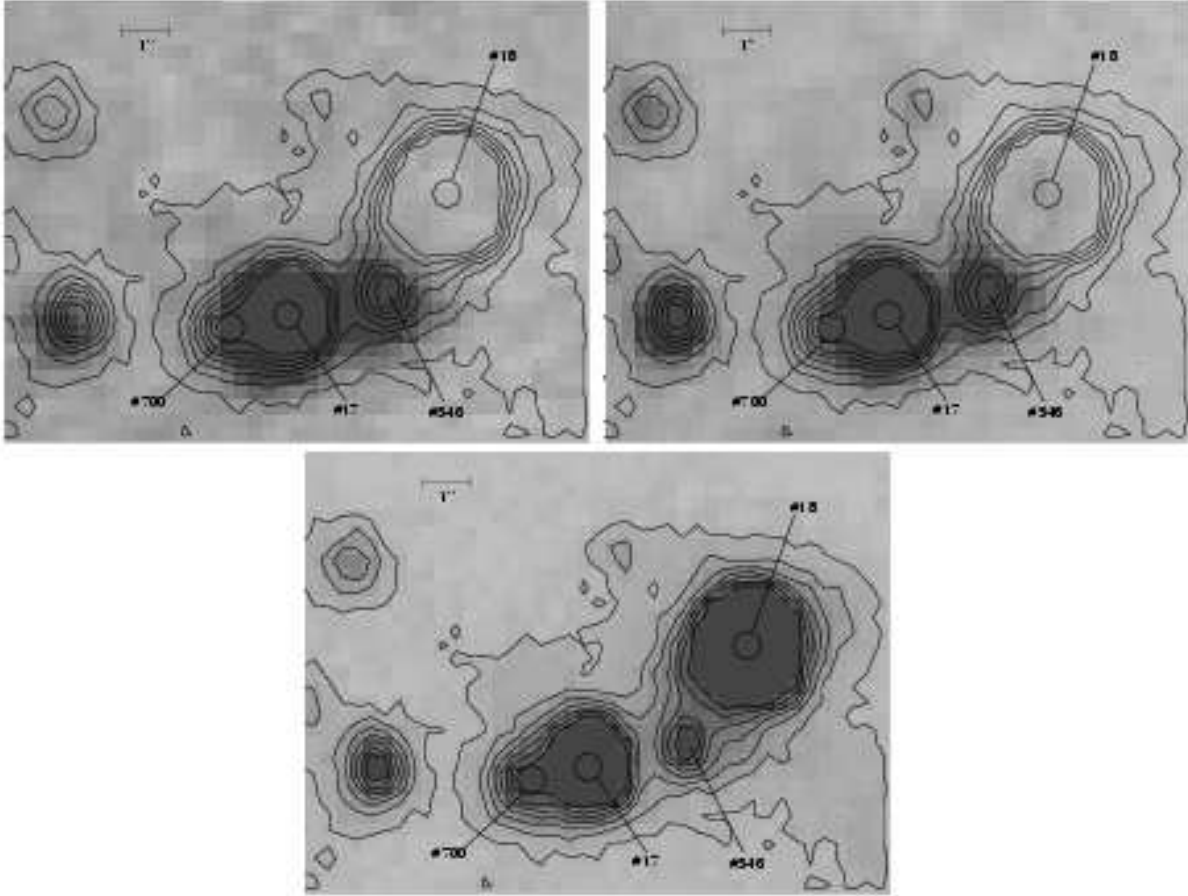


Fig. 10.— *J*, *H* and *K* bands images of G333.1-0.4#18 with contours overplotted to highlight the difference in flux between longer and shorter wavelengths. Object #18 is located at  $\alpha = 16\text{h}21\text{m}02.62\text{s}$  and  $\delta = -50^{\text{deg}}35'54.9''$ .

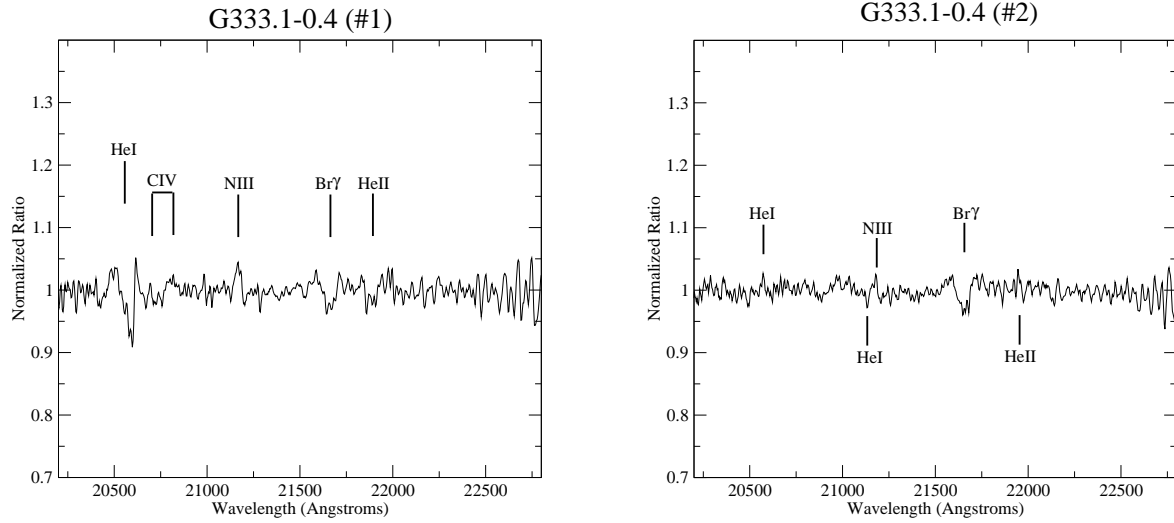


Fig. 11.— *K*-band spectra for the two brightest stars in the G333.1–0.4 cluster: #1 (O6) and #2 (O8V). The two pixel resolution gives  $\lambda/\Delta\lambda \approx 3000$ . Spectra were summed in apertures  $0''.64$  wide by a slit width of  $0''.48$  and include background subtraction from apertures centered  $\leq 1''.0$  on either side of the object. Each spectrum has been normalized by a low-order fit to the continuum (after correction for telluric absorption). The spectra are often contaminated by the  $2.058 \mu\text{m}$  HeI and Br $\gamma$  nebular lines.

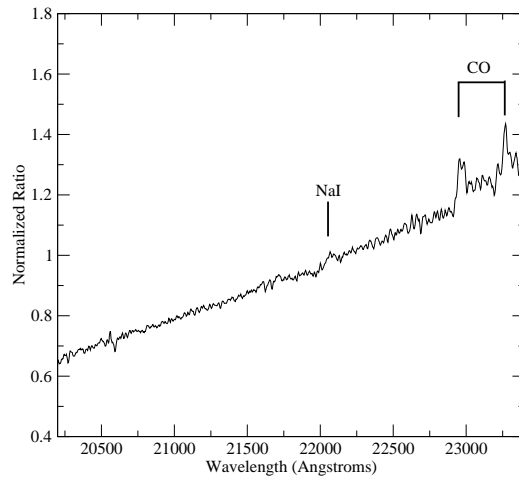


Fig. 12.— *K*-band spectra for G333.1–0.4 #4 displaying featureless continua superimposed on CO emission. A NaI line is present at  $2.207 \mu\text{m}$ .

Table 1. YSO Properties from Photometric Data

ID	$J - H$	$H - K$	$K$	$K$ -excess <sup>a</sup>	$A_K$ <sup>b</sup>	SP Type <sup>c</sup>	Mass <sup>c</sup>
#4	$1.80 \pm 0.02$	$1.44 \pm 0.04$	$10.92 \pm 0.04$	0.35	2.37	O7.5	29
#6	$2.69 \pm 0.02$	$3.28 \pm 0.04$	$11.20 \pm 0.04$	1.67	5.31	O4	70
#9	$2.56 \pm 0.02$	$1.80 \pm 0.04$	$12.08 \pm 0.04$	0.26	2.94	O9	22
#10	$2.26 \pm 0.02$	$1.28 \pm 0.05$	$11.49 \pm 0.04$	-0.08	2.11	O8.5	23
#11	$4.20 \pm 0.05$	$2.46 \pm 0.05$	$11.85 \pm 0.04$	-0.05	4.00	O4.5	58
#13	$3.43 \pm 0.04$	$2.59 \pm 0.04$	$12.28 \pm 0.04$	0.54	4.21	O6.5	34
#14	$2.67 \pm 0.02$	$2.51 \pm 0.04$	$12.19 \pm 0.04$	0.91	4.08	O8	27
#416	$1.10 \pm 0.04$	$1.38 \pm 0.05$	$15.72 \pm 0.05$	0.71	2.27	A7	1.7
#472	$0.26 \pm 0.03$	$1.26 \pm 0.05$	$15.05 \pm 0.05$	1.09	2.08	A5	1.7
#488	$1.77 \pm 0.06$	$2.20 \pm 0.07$	$14.86 \pm 0.04$	1.13	3.58	B4	4
#598	$2.53 \pm 0.07$	$1.89 \pm 0.08$	$10.49 \pm 0.06$	0.38	3.09	O4.5	59

<sup>a</sup>Assuming Koornneef (1983) color for normal stars and that all excess emission is in the  $K$ -band.

<sup>b</sup>Derived reddening after correcting for the excess in the  $K$  band; see §3.4

<sup>c</sup>Properties derived from corrected  $K$  magnitudes, assumed intrinsic colors, and properties of ZAMS or typical OB stars. We obtain the stellar spectral type and mass using the ZAMS properties from Blum et al. (2000); see text.

Table 2. YSO Properties Using Reprocessing Disk Models

ID	$K$ -excess <sup>a</sup>	$A_K$ <sup>b</sup>	SP Type <sup>c</sup>	Mass <sup>c</sup>
#4	2.9	1.57	B4	4
#6	3.5	4.51	B0.5	14
#9	2.8	2.14	B6	3
#10	2.4	1.31	B5	4
#11	3.0	3.2	B2	6
#13	3.0	3.41	B2	5
#14	3.0	3.28	B2	5
#416	1.1	1.47	G0	1
#472	1.3	1.28	F5	1.2
#488	1.7	2.78	A2	2
#598	3.2	2.29	B1	7

<sup>a</sup>Excess emission resulting from a face-on reprocessing disk with a central source corresponding to the spectral type listed in column 4 (Hillenbrand et al. 1992).

<sup>b</sup>Resultant extinction after correcting for the excess  $H - K$  using Hillenbrand et al. (1992) models for reprocessing disks. The  $H - K$  excess is nearly constant and equal to  $\approx 0.5$  mag; see §3.4.

<sup>c</sup>Spectral type and mass obtained from the observed photometric data, extinction correction, excess emission models of Hillenbrand et al. (1992), and ZAMS properties from Blum et al. (2000).

Table 3. O-type Stars Properties

ID	$K^a$	$H - K^a$	$A_K^b$	$D_{ZAMS}^c$	$D_V^c$
#1	$9.16 \pm 0.06$	$0.54 \pm 0.08$	0.94	2.4	3.0
#2	$10.22 \pm 0.04$	$0.57 \pm 0.04$	0.98	2.7	3.9
Average			$0.96 \pm 0.15$	$2.6 \pm 0.4$	$3.5 \pm 0.7$

<sup>a</sup>Uncertainty in photometry is the sum in quadrature of the photometric uncertainty plus the PSF-fitting uncertainty; see §2.)

<sup>b</sup>The uncertainty in  $A_K$  is dominated by the variation in the power-law exponent of the interstellar extinction law ( $\pm 0.16$  - Cardelli et al. 1989); see 3.2. The uncertainty in mean AK is the sum in quadrature of the standard deviation in the mean plus the (0.15 mag) systematic uncertainty due to the extinction law.

<sup>c</sup>Distance estimates assuming mean ZAMS and dwarf (V) luminosities, see text. The uncertainty in the distance is taken as the sum in quadrature of the standard deviation in the mean of the individual estimates plus a component (250 – 500 pc) due to the systematic uncertainty in AK.